Chapter 5

$Ag_3VO_4/CuWO_4$ Z-scheme photocatalysts for Methyl Orange Degradation

5.1. Introduction

Continuous industrialization has led to the discharge of many toxic molecules into the environment, seriously affecting human health and ecological balance (Alsantali et al., 2022; Alvarez et al., 2017; Forgacs et al., 2004; Islam et al., 2023). Among them, organic pollutants seriously threaten the environment because they usually are toxic and non-biodegradable (Hemine et al., 2020; Oller et al., 2011; Saxena et al., 2020). Organic contaminants are generated from chemical industries, household products, paints, indoor furniture coatings, etc. (C. C. Wang et al., 2014). Many environmentally harmful organic dyes like methyl orange (MO) are effluents of textile industries. These compounds are chemically stable and have a potential carcinogenic nature/activity (Katheresan et al., 2018; Lellis et al., 2019). Hence it is essential to find an efficient green technique for degrading these organic pollutants to environmentally benign molecules. Approaches such as adsorption, microwave catalysis, membrane separation, photocatalysis, etc., are different techniques for removing organic contaminants from wastewater (Al-Tohamy et al., 2022; Pandey et al., 2021). Among these, semiconductor-based photocatalysis is a reliable, cost-effective, and efficient technique for degrading organic pollutants in water (D. Zhu & Zhou, 2019).

An efficient photocatalyst for degrading a target organic pollutant should have appropriate valence band (VB) and conduction band (CB) positions with enhanced photo-excited charge separation. Furthermore, the favorable adsorption behavior of the target reactants near appropriate photocatalyst sites is also a requirement. Photocatalysts such as TiO_2 (Lee & Park, 2013), ZnO (Qi et al., 2017), WO_3 (Shandilya et al., 2022), and g-C_3N_4 (Wen et al., 2017) have been applied for the degradation of various organic pollutants. Nevertheless, these single-component photocatalysts suffer from fast recombination of photogenerated charge carriers (Low et al., 2017; H. Wang et al., 2014). Strategies adopted to reduce the recombination rate include doping, metal loading, and the construction of heterojunctions. Composite photocatalysts (heterojunctions) can satisfy the band position, charge separation, and adsorption requirements.

Heterojunctions could follow either the p-n junction or the Z-scheme mechanism (Xu et al., 2018). For the Z-scheme photocatalysts, two n-n type or p-p type semiconductors with staggered band gap positions should be the components for the composite (Low et al., 2017). Given the preceding discussion, the present study investigates a new heterojunction photocatalyst $Ag_3VO_4/CuWO_4$ for pollutant degradation. $CuWO_4$ has a band gap of 2.2-2.4 eV that attributes visible light photocatalytic activity to it (Jatav et al., 2022). Many novel Ag-based photocatalytic materials, such as AgX (X= Cl, Br, I) (Assis et al., 2020), Ag_2CO_3 (J. Li et al., 2015), Ag_3VO_4 (Hu & Hu, 2007), and Ag_3PO_4 (Chen et al., 2015), have been used as promisingly efficient photocatalysts and well-known photosensitive materials in recent years. Among these Ag-based catalysts, Ag_3VO_4 has been shown to have photocatalytic activity owing to its narrow band gap of 2.26 eV and unique band structure (Alshaikh et al., 2021; Kiantazh & Habibi-Yangjeh, 2015). However, the photocatalytic property of pure Ag_3VO_4 was limited due to the high recombination of photogenerated electron-hole pairs (Du et al., 2023). During photocatalytic degradation, silver ions (Ag^+) of Ag_3VO_4 are eventually converted to silver (Ag). Excess Ag will obstruct the active site of Ag_3VO_4, limiting its photocatalytic efficacy (Motora et al., 2020). This significantly reduces the stability of Ag_3VO_4.

Researchers have coupled Ag_3VO_4 with other semiconductors to improve the separation efficiency of photogenerated electron-hole pairs and hence the photocatalytic performance of this promising photocatalytic material. For example, ZnO/Ag_3VO_4 (Kiantazh & Habibi-Yangjeh, 2015), Co_3O_4/Ag_3VO_4 (Zhang, He, Ye, Qin, et al., 2013), TiO_2/Ag_3VO_4/graphene (J. Wang et al., 2013), NiO/Ag_3VO_4

(Ramasamy Raja et al., 2018), $ZnFe_2O_4/Ag_3VO_4$ (Zhang, He, Ye, Wu, et al., 2013), $BiOI/Ag_3VO_4$ (S. Wang et al., 2015), g-C_3N_4/Ag_3VO_4 (S. Wang et al., 2014) and (Q. Zhu et al., 2013) .

Since Ag_3VO_4 has a more negative CB position than $CuWO_4$, this staggered band alignment can facilitate charge transfer from $CuWO_4$ to the CB of the Ag_3VO_4 component in a Z-scheme mechanism. Thus, coupling Ag_3VO_4 with $CuWO_4$ can prevent photo-corrosion disadvantages frequently observed in pure Ag-based semiconductor photocatalysts.

Hence, $Ag_3VO_4/CuWO_4$ composites were prepared via a facile and cost-effective precipitation method. The influence of various parameters on this composite's photocatalytic activity, such as the Ag_3VO_4 to $CuWO_4$ ratio, reaction conditions, etc., were investigated. The synthesized materials were characterized by X-ray diffraction (XRD) and transmission electron microscope (TEM) to investigate phases formed, composite formation, and morphological features/characteristics. The optical properties of the material were investigated by UV-visible diffuse reflectance spectroscopy (DRS) and photoluminescence techniques. X-ray photoelectron spectroscopy (XPS) was used to investigate the chemical composition and the oxidation states of elements in the composite. Photo-excited species trapping experiments gave vital information about the operation of a Z-scheme photocatalysis mechanism.

5.2. Experimental details

5.2.1. Synthesis of $Ag_3VO_4/CuWO_4$

The first step was to re-disperse 1.8 mmol of $CuWO_4$ nanoparticles (preparation given in Chapter 2) in 60 ml double distilled water (DDW) by appropriate sonication. Separately, 0.2 mmol $AgNO_3$ was dissolved in 20 ml DI water. The $AgNO_3$ solution was then added to the $CuWO_4$ nanoparticle dispersion with continuous stirring. The stirring was continued for 24 hours to allow for proper adsorption of Ag^+ ions onto

$CuWO_4$ nanoparticle surfaces. After that, 20 ml of 0.2 mmol of ammonium vanadate solution was poured dropwise into the previously prepared reaction mixture with continuous stirring. The precipitate formed was washed frequently with DDW and ethanol until the pH of the washings turned neutral. Next, the precipitate was dried for 24 hours at 60 °C in a hot air oven. The 10% VW abbreviation represents the finally obtained product. Two more $Ag_3VO_4/CuWO_4$ composites were prepared with 20% and 30% Ag_3VO_4 per mole of $CuWO_4$. These samples are abbreviated as 20% VW and 30% VW in the rest of this chapter (Scheme 5.1).

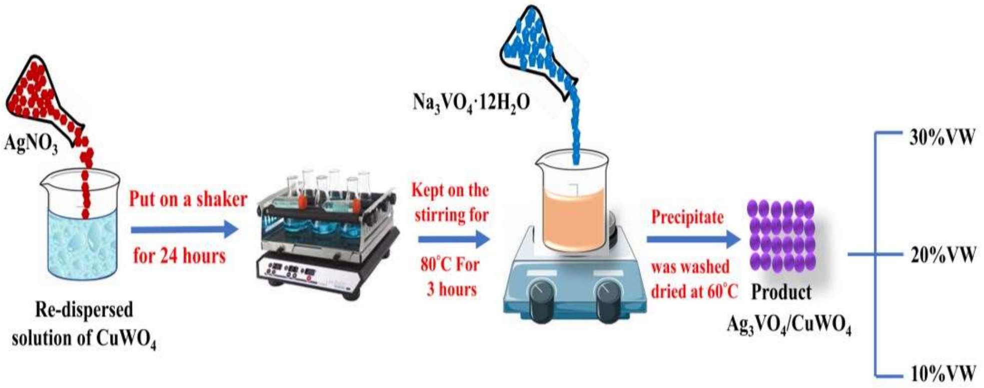

Scheme 5.1: Schematic representation of the preparation of $Ag_3VO_4/CuWO_4$ nanocomposites

5.2.2. Photocatalysis experiments

Photocatalytic activities were evaluated for methyl orange (MO) degradation. Precisely 200 µl of the photocatalyst suspension (0.5 mg/ml) was mixed with an equal volume of MO (2 mg/50ml) in separate cuvettes. The optimum pH of these reaction mixtures was maintained at three and stirred in the dark for 60 min to achieve adsorption-desorption equilibrium. In this process ~5% of MO is adsorbed on catalyst surface. The suspensions in the cuvette (1 cm path length from the source) were kept under cool white LED light (1070 W/m^2). The target reactant (MO) concentration was monitored by UV-visible spectrophotometry at specific time intervals. The following equations calculated the degradation percentage of MO.

$$\text{Removal Efficiency} = \left(\frac{C_o - C_t}{C_o}\right) x 100 \qquad \text{…. (5.1)}$$

In Eq. (5.1), the notation C_0 represents the initial concentration, and C_t is the final concentration.

5.3. Results and Discussion

5.3.1. XRD diffraction pattern

Fig. 5.1 shows the XRD patterns of $CuWO_4$, Ag_3VO_4, and their composites (10% VW, 20% VW, and 30% VW). The XRD of $CuWO_4$ displays major peaks at (2θ) 15.2°, 19°1, 28.6°, 30.1°, 31.6°, 32.1°, and 55.6° (Raizada et al., 2020). These correspond to the (010), (100), $(1\bar{1}\bar{1})$, (111), (020), $(\bar{1}11)$, $(1\bar{1}1)$ planes of the $CuWO_4$ triclinic structure corresponding to the phase documented in JCPDS file 88–0269. The major peaks of Ag_3VO_4 XRD appear at 19.2°, 30.87°, 32.3°, 34.2° and 42.3° (Hu & Hu, 2007). These peaks are indexed to (011), $(\bar{1}21)$, (121), (220), (020), and $(\bar{1}13)$ planes of the Ag_3VO_4 cubic phase (JCPDS file no. 43-0542). The XRD patterns of the composites (10%VW, 20%VW, and 30%VW) have diffraction peaks corresponding to cubic Ag_3VO_4 and triclinic $CuWO_4$.

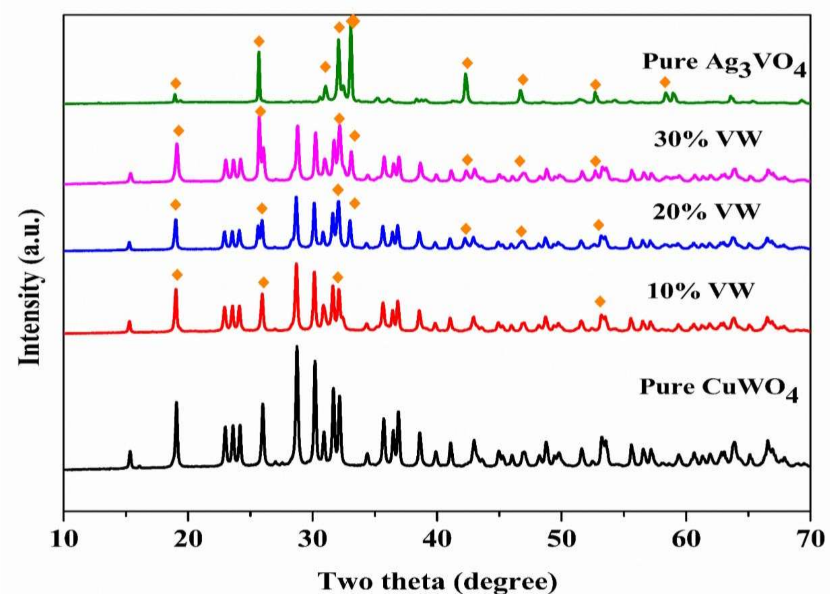

Fig. 5.1: Powder XRD diffraction patterns of the Pure $CuWO_4$, Ag_3VO_4, 10% VW, 20% VW, and 30% VW

5.3.2. TEM analysis

Fig. 5.2 displays the TEM images of $CuWO_4$, 10% VW, and 30% VW. Pure $CuWO_4$ nanoparticles have pentagonal and hexagonal morphologies. The HRTEM image of $CuWO_4$ displays the lattice fringe of 0.269 nm, corresponding to the (110) plane. As demonstrated in a forthcoming section, the 20% VW composite has better photocatalytic activity than the other composites prepared in this study. Considering this, the TEM and HRTEM images of the 20% VW composite sample are presented in Fig. 5.2d and 5.2e. The HRTEM image of 20%VW has two lattice fringes of 0.221 nm and 0.234 nm, corresponding to the $CuWO_4$ (110) and Ag_3VO_4 (100) planes, respectively. The elemental mapping of 20% VW confirms that $CuWO_4$ and Ag_3VO_4 nanostructures are contiguous (Fig 5.3). One deduces that the spherical nanostructures deposited on the surface of $CuWO_4$ are those of cubic Ag_3VO_4 using the above information.

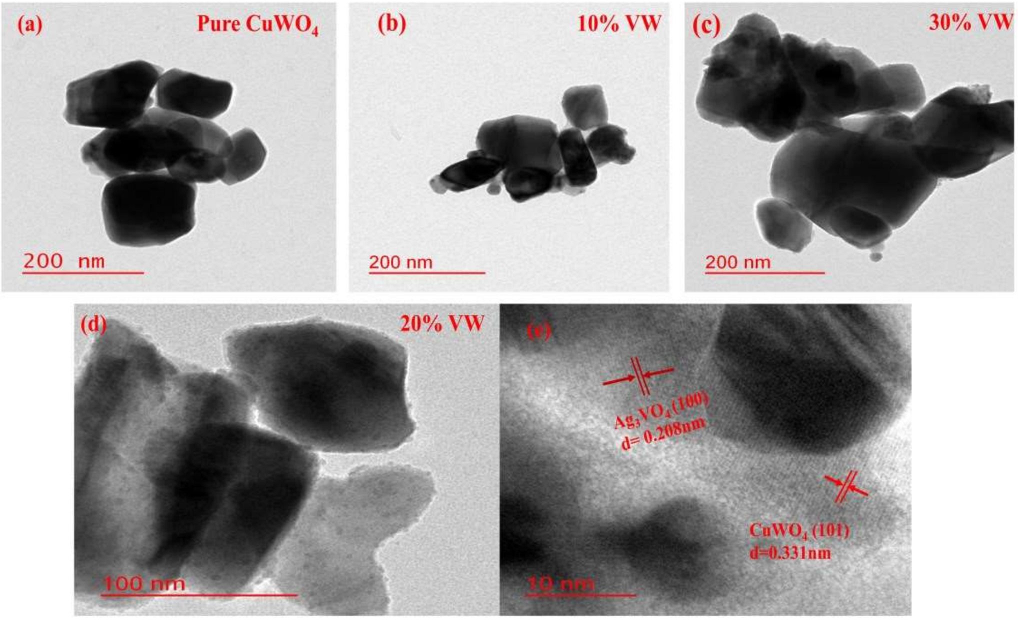

Fig. 5.2: (a)-(d) TEM images of pure $CuWO_4$, 10%VW, 20% VW, and 30% VW and (e) HR-TEM images of 20% VW

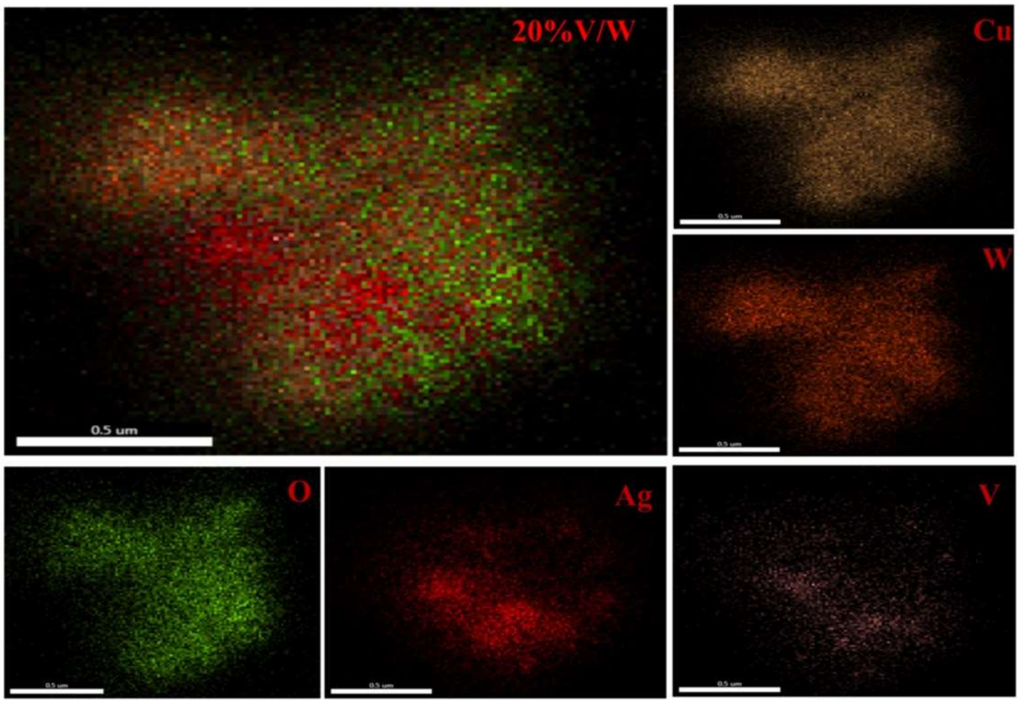

Fig. 5.3: Elemental mapping of 20% V/W nanostructures

5.3.3. XPS Analysis

XPS was used to identify the elements present in samples and their oxidation states. The C1s peak at 284.4 eV was used to calibrate the XPS binding energies of all samples. Fig. 5.4 shows the survey spectra of samples $CuWO_4$, Ag_3VO_4, and their composites. These were further analyzed at higher resolutions to investigate the finer features of the respective spectrums. Fig. 5.5 compares high-resolution peaks corresponding to an element in the pure phase (Ag_3VO_4 or $CuWO_4$) and its spectrum as part of the 20% VW sample. Thus, Cu $_{2p3/2}$ and Cu $_{2p1/2}$ peaks of the $CuWO_4$ sample are at 933.9 eV and 953.6 eV. In contrast, the binding energies corresponding to Cu $_{2p3/2}$ and Cu $_{2p1/2}$ peaks increase to 934.5 and 954.4 eV, respectively, for the 20% VW composite. Similarly, the W_{4f} peaks at 35.1 and 37.3 eV (ascribed to the W^{+6} oxidation state) in $CuWO_4$, increase to 35.3 and 37.6 eV in the 20%VW spectrum.

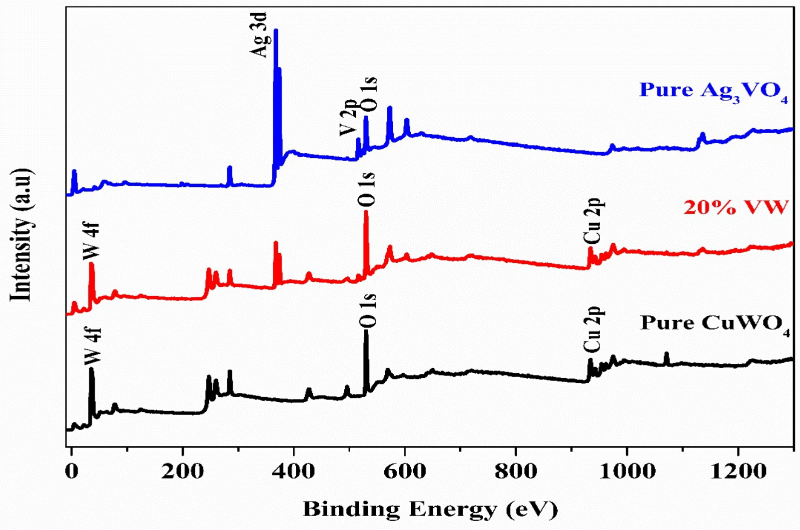

Fig. 5.4: Survey spectrums of as-prepared samples pure $CuWO_4$, Ag_3PO_4, and 20% VW

The Ag3d ($Ag3d_{3/2}$ and $Ag3d_{1/2}$, respectively) binding energies of Ag_3VO_4 appear at 368.3 and 374.3 eV. These peaks red-shift to 368 and 374.1 eV in the XPS spectrum of the composite 20%VW. One can see two O1s peaks in the XPS of Ag_3VO_4 and the 20%VW composite. The Ag_3VO_4 (O1s) spectrum peaks are at 530.2 and 532.3eV. However, there is only one O1s peak (at 530.2 eV) in the spectrum of $CuWO_4$. These peaks shift to 530.3 and 531.3 eV in the 20%VW spectrum. The first peak at 530.2 (shifts to 530.3 eV for the composite) is due to lattice oxygen. The water molecule was responsible for the peaks at 531.2 eV, while the peak at 532.3 eV (in Ag_3VO_4) is attributed to chemisorbed oxygen (Yan et al., 2015).

The $V2p_{3/2}$ and $V2p_{1/2}$peaks (XPS of Ag_3VO_4) observed at 516.8 eV and 524.2 eV are due to the +5 oxidation state of vanadium. The same peaks of V_{2p} shift to 516.7 eV and 523.9 eV in the 20%VW composite. Overall, the XPS of 20% VW displays a positive shift from $CuWO_4$ and a negative shift of binding energies from Ag_3VO_4. Thus, there is a net migration of charge carriers from $CuWO_4$ to Ag_3VO_4 in the composite. Such a charge transfer indicates the operation of a Z-scheme mechanism.

Fig. 5.6a and 5.6b give the valence band (VB) edge XPS spectra of $CuWO_4$ and Ag_3VO_4. The Ag_3VO_4 VB edge (E_{VB}) is at 1.26 eV, while that of $CuWO_4$ is at 1.56 eV.

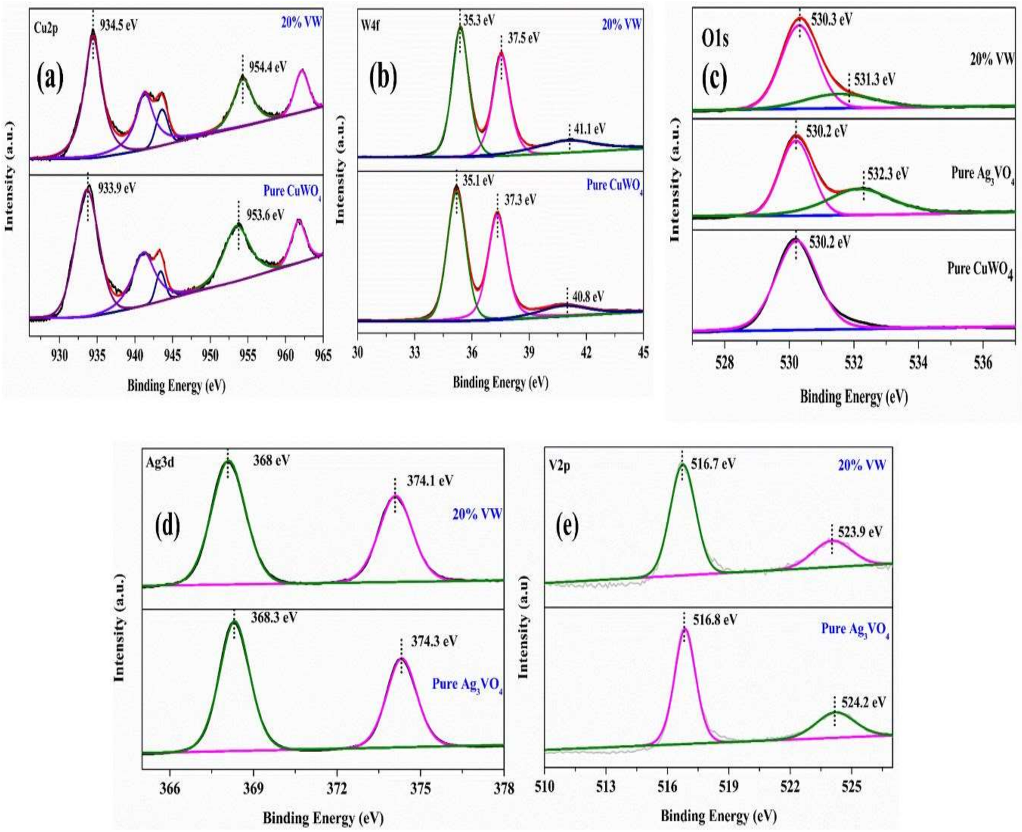

Fig. 5.5: Comparison between HR-XPS spectrums of different regions of 20 % VW with the spectrums of Ag_3VO_4 and $CuWO_4$ (a) Cu2p (b) W1s (c) O 1s (d) Ag 2p (e) V 2p

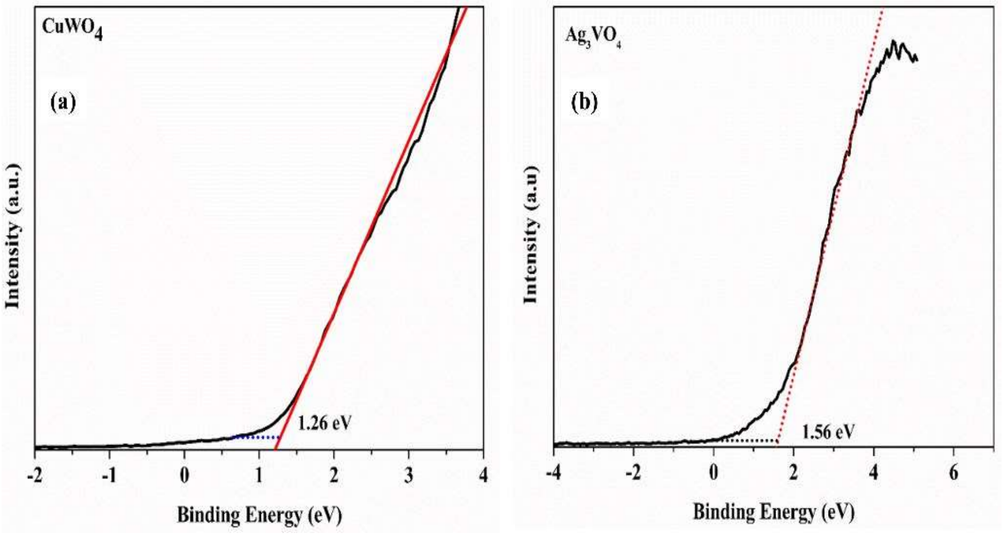

Fig. 5.6: The valence band spectra of (f) $CuWO_4$ and (g) Ag_3VO_4

5.3.4. UV-DRS Analysis

Fig. 5.7 displays the solid-state absorbance plots of nanoparticle samples prepared in this study. The absorption band edge of $CuWO_4$ is at 530 nm, while Ag_3VO_4 is at 550 nm. In contrast, Fig. 5.7b shows the Tauc plots for $CuWO_4$ and Ag_3VO_4 nanoparticles. The band gap of $CuWO_4$, Ag_3VO_4, and their nanocomposites are calculated by the Tauc plot equation(5.7).

$$(\alpha h\upsilon)^{1/n} = (h\upsilon - E_g) \qquad (5.2)$$

In equation (5.2), α is the molar absorption coefficient, h is Planck's constant, υ is the incident photon frequency, and E_g is the semiconductor band gap. The value n equals 2 for indirect allowed transition and 1/2 for direct transition. Both $CuWO_4$ and Ag_3VO_4 fit the indirect band gap Tauc plots. The indirect band gaps of $CuWO_4$ and Ag_3VO_4 are ~ 2.3 and 2.4 eV. Equation (5.3) gives the two semiconductor components' conduction band (CB) positions (E_{CB}).

$$E_{CB} = E_{VB} - Eg \qquad (5.3)$$

As mentioned earlier, the E_{VB} positions of the $CuWO_4$ and Ag_3VO_4 were determined from respective VB-XPS spectra. The E_{CB} of pure $CuWO_4$ and Ag_3VO_4 found from equation (2) are -1.04 and -0.84 eV, respectively.

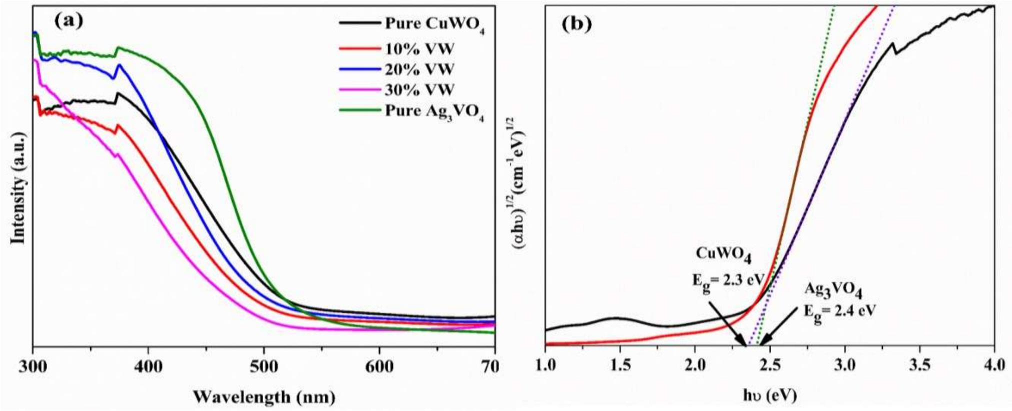

Fig. 5.7: (a) The solid-state UV − vis absorption spectrum of the nanomaterials prepared in this study. The $(\alpha h\nu)^2$ vs. energy hν Tauc plots and bandgap energy of the pure (b) $CuWO_4$ and Ag_3VO_4 nanoparticles.

5.3.5. Photoluminescence

The PL analysis investigates the relative charge carrier recombination kinetics. As lower the PL peak intensity, the slower the recombination kinetics or better charge separation (Jatav et al., 2022). Fig. 5.8 shows the PL spectra of Pure $CuWO_4$, Ag_3VO_4, and their composites (10% VW, 20% VW, and 30% VW). Sample 20% VW shows lesser intensity than other prepared samples, indicating a slower recombination rate of electrons and holes. It also points to improved charge transfer between $CuWO_4$ and Ag_3VO_4 components in the 20% VW sample.

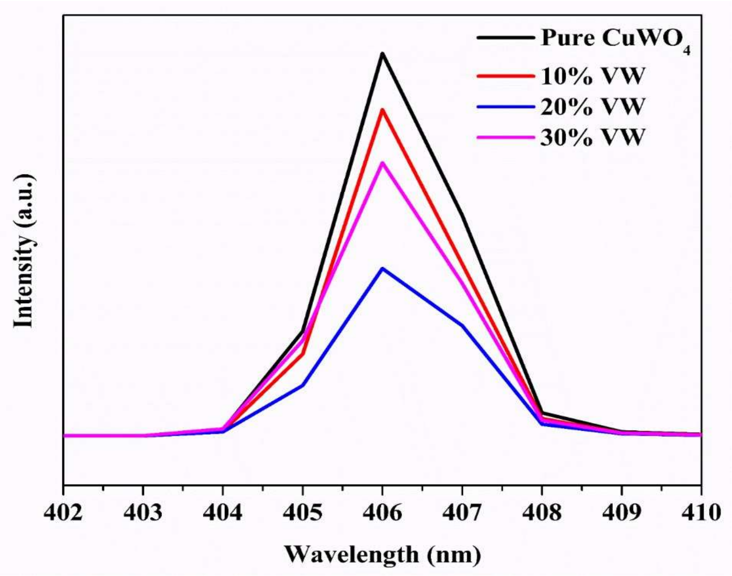

Fig. 5.8: Photoluminescence spectra of the prepared samples.

5.3.6. Photocatalytic Activity

The photocatalytic activities of as-prepared samples were tested for the degradation of MO under visible light irradiation. Blank experiments were performed by placing MO solution under visible light irradiation without any photocatalyst. Photodegradation in this condition was negligible for MO. As mentioned in sub-section 5.2.2, the target organic molecule (MO) solution and the photocatalyst dispersion were mixed and kept in the dark for a prolonged period until achieving adsorption-desorption equilibrium. Fig. 5.9a shows the change in UV-visible spectra of MO with their degradation. Fig. 5.9b displays plots of MO degradation using different photocatalysts with the time of visible light irradiation. The 20% VW composite exhibits better photocatalytic activity than $CuWO_4$, Ag_3VO_4, 10% VW, and 30% VW nanomaterials. Nearly complete (~90%) MO degradation occurred on 20% VW, while 60% and 30% degradation happened on the 10% VW and 30% VW photocatalysts. Degradation of MO was minimal when $CuWO_4$ and Ag_3VO_4 nanoparticles were used as the photocatalysts with the same visible light exposure time. The kinetics of the photocatalytic degradation of the target organic molecules were also studied.

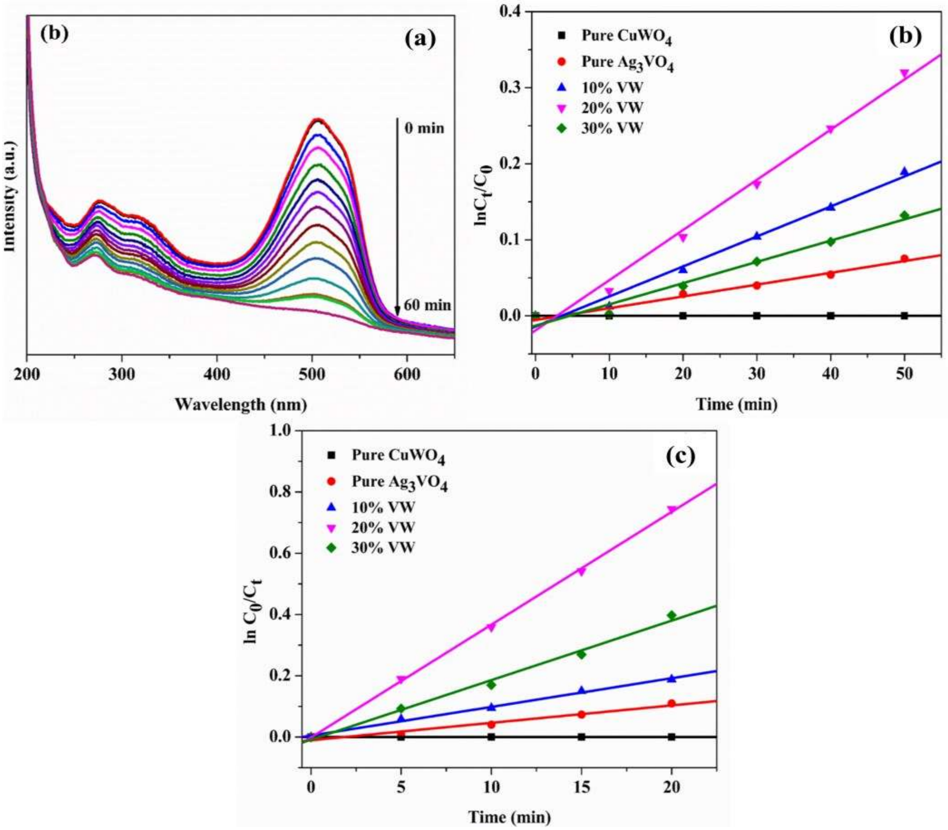

Fig. 5.9: (**a**) UV-visible spectra of MO versus time on the 20% VW catalyst, (b) change in normalized MO concentration with visible light exposure time on the nanomaterials prepared in this study, and (c) pseudo-first-order kinetics plots of MO degradation on $CuWO_4$, Ag_3VO_4, and their nanocomposites.

Fig. 5.9c shows the photocatalytic degradation of MO with time. It follows pseudo-first-order kinetics. Thus, the $\ln(C_t/C_0)$ data points versus the time plot have a linear fit with the slope or rate constant *k*. Here, C_0 is the initial concentration of the target organic pollutant, C_t is the concentration at time *t*, and *k* is the rate constant. The details of kinetic studies for MO degradation have been given in Table 5.1.

Table 5.1: Rate constant (*k*) and correlation coefficient (R^2) of MO degradation on pure $CuWO_4$, Ag_3VO_4, 10% VW, 20% VW, and 30% VW photocatalysts

Catalysts	Rate constant (min^{-1})	R^2
Pure $CuWO_4$	0.0001	1
Pure Ag_3PO_4	0.0029	0.998
10% AW	0.0069	0.995
20% AW	0.0009	0.997
30% AW	0.0037	0.967

Table 5.2 compares turnover frequency (TOF) values of MO degradation on previously reported vanadium or tungsten-based photocatalysts. The MO degradation TOF of 20%VW is among the best reported to date.

Table 5.2: Comparison of MO degradation turnover frequency (TOF) values over different photocatalysts with 10% MW

Photocatalysts	Light source	Turnover frequency ($mol.g^{-1}.min^{-1}$)	References
$ZnFe_2O_4/Ag/Ag_3VO_4$	300W Xe lamp	0.05×10^{-3}	(Jing et al., 2017)
Ag_3VO_4/TiO_2/graphene	500W Xe lamp	1.1×10^{-3}	(J. Wang et al., 2013)
Ag_3VO_4/Bi_2WO_6	300W Xe lamp	1.5×10^{-3}	(S. Li et al., 2017)
$Ag_3VO_4/CuWO_4$	Cool white LED ($1070\ W/m^2$)	2.4×10^{-3}	Our Work

5.3.7. Recyclability

Fig. 5.10a gives the recyclability graph of the 20% AW photocatalyst for MO degradation. Note that the reaction conditions were the same for all cycles. The recyclability of the photocatalyst was quite good for MO degradation. By the fifth cycle, the photocatalytic activities decreased to nearly 85% of the first cycle activities for both MO degradation. Fig. 5.10b compares the XRD patterns of the recycled and freshly prepared 20% VW samples. The diffraction pattern of the recycled material displays all the peaks observed for the fresh 20% VW sample. Thus, the 20% VW sample has good photostability even after five reuse cycles.

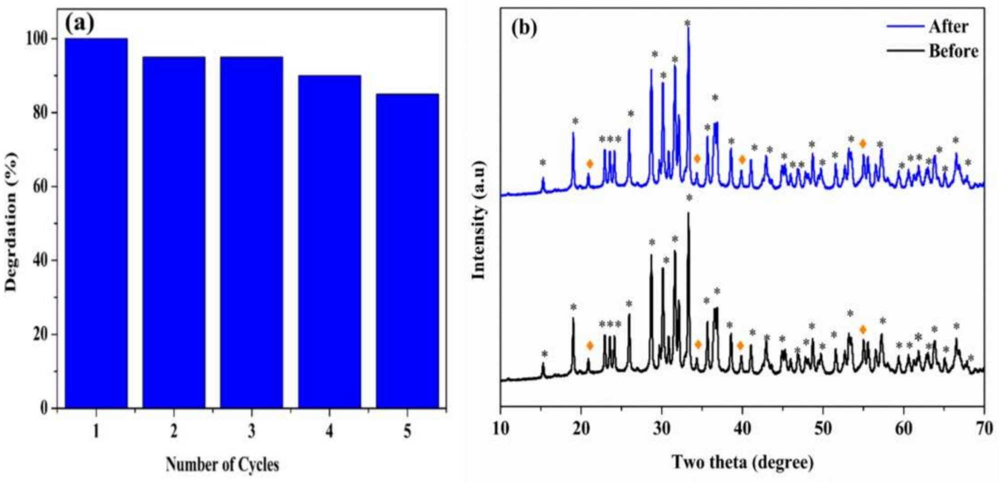

Fig. 5.10: **(a)** Recyclability of MO degradation over 20% VW, (**b**) XRD after recyclability

5.3.8. Photocatalysis with scavenger molecules

Radical scavengers play an important role in the photocatalytic degradation of dyes (MO). Separate experiments were conducted with scavengers for specific reactive species. Isopropyl alcohol (IPA) was the $^{\bullet}OH$ scavenger, KI was the hole scavenger, and PBQ was the superoxide radical scavenger used with 20% VW photocatalysts. Fig. 5.11 shows the reaction carried out under visible light with or without a scavenger. Reaction conditions were the same in all the experiments. The first bar denotes the blank experiment, meaning the experiment was carried out without a scavenger and set as the benchmark assumed to be 100%. The rest of the bars in the histogram are the relative percentages (compared to the first one) of degradation under visible light in the presence of KI, IPA, and PBQ. One can see that KI has the maximum inhibiting effect on the photocatalysis of MO. PBQ also slows down MO degradation kinetics, but the effect is lesser than KI. The results imply that photoexcited holes are the main reactive species generated during the reaction on the 20% VW nanocomposite. Moreover, direct MO oxidation on CB through superoxide radicals is also a viable degradation pathway. IPA has very little effect on MO photocatalytic degradation.

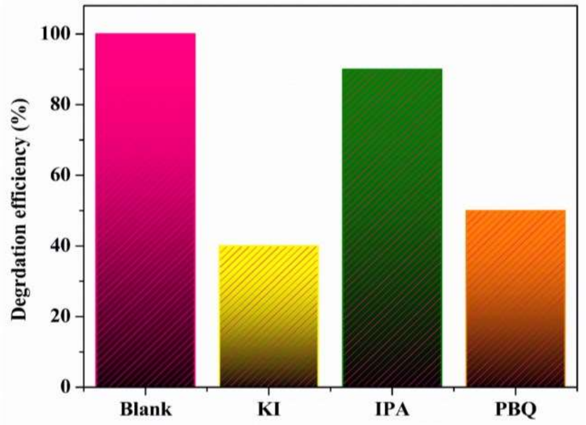

Fig. 5.11: The species trapping experiment for MO degradation over 20% VW

5.3.9. Photocatalytic Mechanism

A Z-scheme mechanism has been proposed based on the above experimental results. Visible light irradiation on the 20% VW nanocomposite photoexcites both $CuWO_4$ and Ag_3VO_4 components. The photo-excited electrons from the CB of $CuWO_4$ recombine with the photogenerated holes in the VB of Ag_3VO_4. Thus, the holes get concentrated in the $CuWO_4$ VB, while the photo-excited electrons are located on the Ag_3VO_4 CB. Photoexcited electrons react with adsorbed oxygen to produce superoxide radicals. The results of scavenger photocatalysis experiments validate this mechanism. XPS results also demonstrate the migration of charges from $CuWO_4$ to Ag_3VO_4. The migration of electrons from $CuWO_4$ to Ag_3VO_4 suppresses electron-hole recombination, increasing photocatalytic efficiency. PL spectra studies also show that electron-hole recombination is lesser in the 20% VW photocatalyst. MO molecules get oxidized by their direct oxidation on $CuWO_4$ VB. Then, the superoxide radicals produced on the CB provide another pathway for MO oxidation (Fig 5.12).

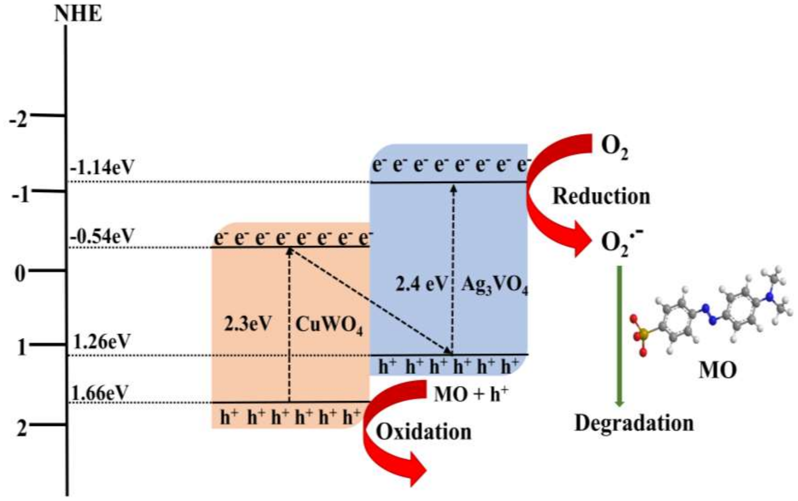

Fig. 5.12: The possible photocatalytic mechanism of organic pollutant degradation on the 20% VW photocatalyst

5.4. Conclusions

$CuWO_4$ and Ag_3VO_4 are both photocatalysts with visible range band gaps. Given this, three composites with varying amounts of Ag_3VO_4 precipitation on $CuWO_4$ were prepared. XPS analysis showed charge transfer from the $CuWO_4$ side to the Ag_3VO_4 part. The 20% VW sample demonstrated the best photocatalytic activity for MO degradation. All photocatalysis experiments were carried out under an economical visible light LED bulb. The turnover frequency for the organic pollutant degradation (using an LED light source) on the 20% VW is among the best values reported for W-based photocatalysts in the literature. The 20% VW sample also demonstrates appropriate recyclability up to five cycles of its reuse. The target organic pollutant (MO) was degraded mainly by photo-excited holes and direct oxidation with superoxide radicals.